First-Principles-Based Insight into Electrochemical Reactivity in a Cobalt-Carbonate-Hydroxide Pseudocapacitor

Kenji Oqmhula,* Takahiro Toma, Ryo Maezono, and Kenta Hongo*

ABSTRACT: Cobalt carbonate hydroxide (CCH) is a pseudocapacitive material with remarkably high capacitance and cycle stability. Previously, it was reported that CCH pseudocapacitive materials are orthorhombic in nature. Recent structural characterization has revealed that they are hexagonal in nature; however, their H positions still remain unclear. In this work, we carried out first-principles simulations to identify the H positions. We then considered various fundamental deprotonation reactions inside the crystal and computationally evaluated the electromotive forces (EMF) of deprotonation (V_{dp}). Compared with the experimental potential window of the reaction (<0.6 V (vs saturated calomel electrode (SCE)), the computed V_{dp} (vs SCE) value (3.05 V) was

H-bond-driven 1D crystal growth

beyond the potential window, indicating that deprotonation never occurred inside the crystal. This may be attributed to the strong hydrogen bonds (H-bonds) that formed in the crystal, leading to structural stabilization. We further investigated the crystal anisotropy in an actual capacitive material by considering the growth mechanism of the CCH crystal. By associating our X-ray diffraction (XRD) peak simulations with experimental structural analysis, we found that the H-bonds formed between CCH $\{(\bar{1}\bar{1}\bar{1}), (2\bar{1}\bar{1}), (2\bar{1}1)\}$ planes (approximately parallel to the ab-plane) can result in 1-D growth (stacked along the c-axis). This anisotropic growth controls the balance between the total "non-reactive" CCH phases (inside the material) and the "reactive" hydroxide $(Co(OH)_2)$ phases (surface layers); the former stabilizes the structure, whereas the latter contributes to the electrochemical reaction. The balanced phases in the actual material can realize high capacity and cycle stability. The results obtained highlight the possibility of regulating the ratio of the CCH phase versus the $Co(OH)_2$ phase by controlling the reaction surface area.
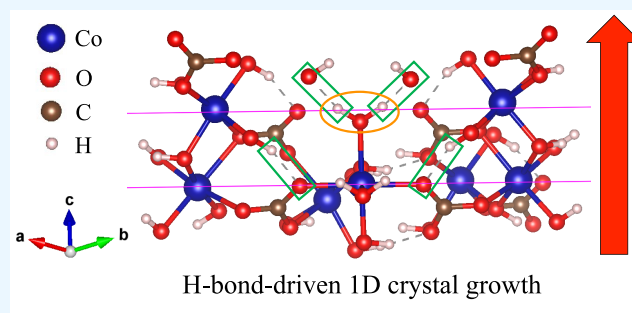
1. INTRODUCTION

For clean energy applications, pseudocapacitors with Co-based anodes can be applied to large-scale power storage devices with excellent characteristics, such as fast charge—discharge behavior, long life, and high capacity.[1,2] Because of the balance between high capacity and cycle stability, cobalt carbonate hydroxide (CCH)[3,4] has recently attracted increasing attention compared to conventional Co-based anode materials, such as cobalt oxide (Co_3O_4),[5,6] cobalt hydroxide $(Co(OH)_2)$,[7,8] mixtures of cobalt carbonate and cobalt oxide $(CoCO_3/CoO)$,[9] and hybrid materials of ionic liquids and $Co(OH)_2$.[10] In fact, it has been reported that a pristine CCH anode exhibits low capacity.[11] In addition, the "high-capacity CCH anode" is not obtained from CCH itself, but from $Co(OH)_2$ formed in the CCH via calcination,[3,11,12] although the CCH contributes to high cycle stability due to its robust/resilient structure against the electrochemical reaction. XRD experiments have suggested the existence of mixed phases consisting of CCH and $Co(OH)_2$.[3,11] In charge—discharge cycles of the "high-capacity CCH anode," Co(II) and Co(III) states have been observed alternatively, suggesting that $Co(OH)_2$ is deprotonated to CoOOH, followed by deprotonation to CoO_2, and *vice versa*.

The electrochemical reaction in $Co(OH)_2$ has been investigated through first-principles simulations,[5] thus providing atomistic insights into the detailed mechanism. Analogous to this, it has been proposed that the above-mentioned two-step reaction is attributed to the high capacity of the CCH anode.[3,11,12] The above-mentioned reaction mechanism can be considered as plausible, but hypothetical; that is, there is no evidence of electrochemical reactions in the CCH anode at the atomic level because the CCH crystal structure still remains unclear.[4,13] Therefore, similar first-principles/atomic-level simulations have not yet been applied.

In high-capacity CCH anodes, their morphologies strongly affect their capacitance, i.e., capacity and cycle life. The best capacitance, so far, has been achieved with a CCH anode possessing an umbrella-like morphology controlled by the
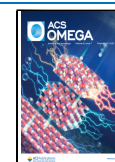
crystal growth time.[3,4] This anode material has a well-controlled 1-D anisotropic morphology, including well-balanced CCH and $Co(OH)_2$ phases; the former is responsible for the structural stability (i.e., long life cycle), while the latter is responsible for the high capacity. Therefore, the morphology of the CCH anode balancing CCH and $Co(OH)_2$ phases is critical for achieving outstanding capacitance properties. The morphology of CCH can be controlled by the crystal growth direction; more 1-D anisotropic morphology results in less CCH phase/more $Co(OH)_2$ phase, thereby leading to a larger reactive area and, hence, higher capacity. This anisotropy can be controlled by the packing ratio of carbonate ions in the crystal. However, the reason behind the carbonate ion's contribution to crystal growth is still unclear, because there is no detailed information on the atomic positions in the CCH crystal structure at present.

Thus, accurately identifying the CCH crystal structure is the first step toward achieving a deeper understanding of "high-capacity" CCH anodes.

For instance, if the position of carbonate ions is known, we should be able to consider the deprotonation site of the hydroxide phase formed by calcination. The CCH compound includes carbonate and hydroxide ions as well as hydrated water; its crystal structure is much more complex than those of oxides and hydroxides. Previously, an XRD analysis assuming an orthorhombic lattice identified the CCH compound as $Co(OH)(CO_3)_{0.5} \cdot 0.11H_2O$ (JCPDS 48-0083).[14] However, recent sophisticated experiments have suggested that CCH is actually $Co_6(CO_3)_2(OH)_8 \cdot H_2O$ with a hexagonal lattice.[4,13] The crystal system has been identified, but detailed information about atomic positions has yet to be explored as it is quite difficult to identify hydrogen (by neutron diffraction) and Co vacancy positions.

This study aims (i) to accurately identify the CCH crystal structure and (ii) to elucidate the relationship between the material morphology and the crystal growth; the first addresses the "bulk" aspect, whereas the second addresses the "material" aspect in a pseudocapacitor. Based on the resulting structures, we systematically investigated the capacitance properties of the CCH anodes (reductant), referring to those reported in previous studies. The EMF of the CCH anodes was evaluated via first-principles simulations to investigate electrochemical reactivity. We found that the CCH crystal forms H-bond networks that contribute to cyclic stability; the H-bond inhibits the deprotonation reaction in the CCH crystal. Eventually, we concluded that the reaction site cannot be attributed to the CCH phase but is attributed to the $Co(OH)_2$ phase; CCH can be considered as the precursor of the $Co(OH)_2$ phase, with a wire-like morphology. To identify the crystal planes that contribute toward crystal growth, we performed XRD peak simulations on the resultant crystal structure with a hexagonal lattice and assigned the plane indices. We found that the H-bonds formed between the $\{(\bar{1}\bar{1}\bar{1}), (2\bar{1}\bar{1}), (2\bar{1}1)\}$ planes contribute toward 1-D crystal growth.

This paper is organized as follows: Section 2 starts with the modeling of the CCH crystal structure to identify hydrogen and Co defect positions therein; to evaluate the EMF of the reaction using first-principles simulations, we hypothesized the CCH electrode reaction (deprotonation) based on the structural modeling of the oxide (dehydrogenation location identification), followed by the present first-principles simulations. In Section 3, the results of this work are presented, i.e., identification of the reductant structure, the oxidant structure to evaluate the EMFs of the deprotonation, and the XRD

simulation to assign the peaks to the correct Miller indices. According to the results obtained, Section 4 provides new insights into the storage performance of CCH-based electrodes. The conclusions drawn from the findings are provided in Section 5.

2. METHODOLOGIES

2.1. Outline. Exhaustive first-principles simulations for all possible atomic configurations were carried out, and the CCH structures in reduced and oxidized forms were identified as the most stable structures. The electrochemical reactivity of the CCH anode was evaluated from the EMF value, which is defined as the energy difference between the reductant and oxidant. Furthermore, their structural changes provide critical information for understanding the cycle performance because they correlate well with each other.[8,15,16] The structural and computational modeling are outlined as follows:

(i) According to the recent experiments on structural characterization of CCH anodes,[4,13] we considered the CCH reductant to be $Co_6(CO_3)_2(OH)_8 \cdot H_2O$ in the hexagonal $P\bar{6}2m$ space group (No. 189); however, its Co defect (V_{Co}) and H positions have not yet been determined experimentally. (See Subsection 3.1.) This indicates that there are several possible arrangements of the V_{Co} and H positions therein. First-principles simulations are well-known for identifying unknown atomic positions in disordered structures.[17] Therefore, we exhaustively applied first-principles simulations to all the possible arrangements, identifying the reductant structure as the most stable one. (See Subsection 2.5.)

(ii) To theoretically elucidate the electrochemical properties of the CCH anode, the most reliable approach is first-principles reaction dynamics simulations. However, due to their high computational cost, such simulations are not feasible. Instead, the present study adopted a static approach; that is, we evaluated the EMF. To evaluate the oxidant energy, the oxidant structure should be modeled, but this modeling involves assuming a plausible electrochemical reaction. Before modeling the oxidant structure, we reviewed the electrochemical reactions, which are hypothetically assumed as deprotonation reactions.[3,4,11,12] (See Subsection 2.3.)

(iii) According to the hypothetical reaction mechanism, we can model the oxidant structure by deprotonating the reductant structure. (See Subsection 2.4.) By applying first-principles simulations to both the reductant and oxidant structures, the EMF (V_{dp}) can be calculated from their energy difference computed using first-principles geometry optimization. (See Subsection 2.5.) Upon comparing the predicted V_{dp} with the experimental values, we verified the reaction hypothesis.

(iv) Actual CCH anodes have 1-D wire structures rather than 3-D bulk structures.[3,4,11,12] Therefore, we considered the anisotropic morphologies of the CCH anodes to understand "actual" capacitor properties from a more realistic viewpoint. The crystal growth mechanism can govern the morphology. The anisotropy of the crystal growth can be measured from the XRD pattern; the crystal grows toward crystal planes that correspond to higher peak intensities in its XRD pattern.[18] In fact, previous characterizations of the CCH anodes were incorrect because they were characterized by assuming a lattice structure with an

incorrect space group.[14] Therefore, we performed XRD simulations[19] for our predicted CCH reductant structure to obtain the accurate attribution of the XRD patterns to crystal planes. (See Subsection 2.6.) This revised XRD attribution can lead to the correct crystal growth mechanism. In addition, the detailed structural information about carbonate ions and surrounding atoms clarifies the interactions between them. This detailed information can provide new insights into the morphology of the CCH anode and hence its electrochemical reactivity governing the capacitor properties, i.e., high capacity and cycle stability.

2.2. Modeling of CCH Reductant Structure.
Figure 1 shows a unit cell of $Co_6(CO_3)_2(OH)_8 \cdot H_2O$ obtained from
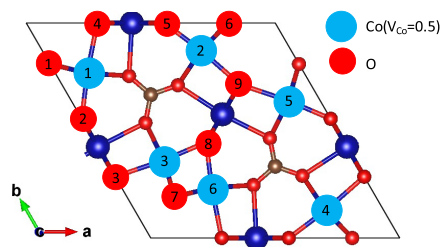
Figure 1. Unit cell in the *ab* plane. Atomic positions colored by light blue and red are six Co-defective (V_{Co}) sites with a site occupancy number of 0.5 and nine O sites that bond with H atoms, respectively. Three of the V_{Co} sites and one of the O sites exist as vacancies and structural water, respectively.

experimental characterization,[13] which was the starting point of our structural modeling. Its lattice information (lattice parameters and space group) was identified, but the atomic positions therein are incomplete from the viewpoint of the Co-defect (V_{Co}) and H positions. The atomic positions of Co, O, and C were identified, but there exist six Co positions with site occupancy numbers of 0.5 (light blue). This means that three Co positions are fully occupied and the remaining three are V_{Co} positions. Ten H atomic positions were categorized into eight OH sites and one structural water (H_2O) site. Through first-principles simulations shown later, the structural model of the reductant was determined by choosing the most stable structure from all the possible arrangements of the V_{Co} and H positions. As shown below, we identified (i) the V_{Co} and (ii) H positions considering physicochemically reasonable arrangements.

(i) Identification of the V_{Co} positions: The vacancy patterns can be divided into two categories: (1) delocalized and (2) localized. According to the symmetry of the V_{Co} patterns, we have two delocalized patterns, (1-1) $V_{Co}(2/3/5)$ and (1-2) $V_{Co}(1/2/3)$, and two localized ones, (2-1) $V_{Co}(2/3/4)$ and (2-2) $V_{Co}(3/5/6)$, where the three V_{Co} positions are described in parentheses as numbers in Figure 1.

(ii) Identification of the H positions: For each of the above four V_{Co} patterns (1-1) ~ (2-2), the H positions can be automatically determined if one H_2O position is chosen from nine O positions, $W_O(l)$ ($l = 1-9$), appearing in Figure 1. Furthermore, as explained below, we consider their symmetries and impose constraint conditions from the viewpoint of the local charge neutrality such that isolated anions are ruled out in the reductant, and thus, 14 candidate structures are left, described as $V_{Co}(i/j/k)$-$W_O(l)$:

(1-1) $V_{Co}(2/3/5)$-$W_O(l)$ ($l = 1-9$): As can be seen from Figure 2(a), this case allows all the nine O sites because neither symmetry nor local charge neutrality rules out any W_O possibility.
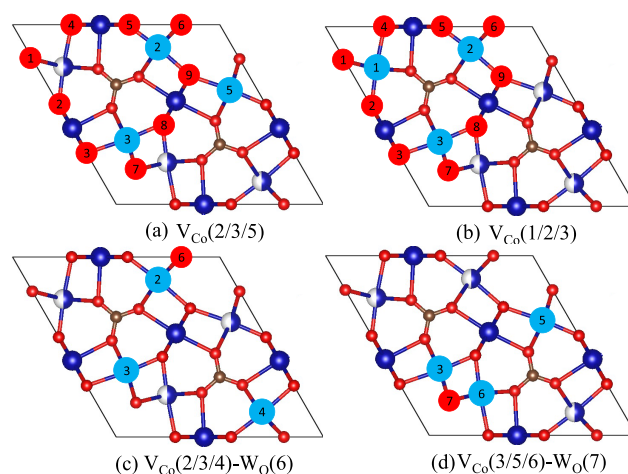
Figure 2. Possible structural models of $V_{Co}(i/j/k)$-$W_O(l)$, where V_{Co} and structural water positions are colored by light blue and red, respectively: (a) nine possible patterns, $V_{Co}(2/3/5)$-$W_O(l)$ ($l = 1-9$), (b) three possible patterns, $V_{Co}(1/2/3)$-$W_O(l)$ ($l = 1, 2, 3$), (c) one unique pattern, $V_{Co}(2/3/6)$-$W_O(6)$, and (d) $V_{Co}(3/5/6)$-$W_O(7)$.

(1-2) $V_{Co}(1/2/3)$-$W_O(l)$ ($l = 1, 2, 3$): Figure 2(b) shows that $V_{Co}(1/2/3)$ has a 3-fold symmetry; therefore, $W_O(l)$ are classified into three equivalences: {$W_O(1)$, $W_O(6)$, $W_O(7)$}, {$W_O(2)$, $W_O(5)$, $W_O(8)$}, and {$W_O(3)$, $W_O(4)$, $W_O(9)$}. Therefore, we may consider only three inequivalent $W_O(l)$ ($l = 1, 2, 3$).

(2-1) $V_{Co}(2/3/4)$-$W_O(6)$: Looking at Figure 2(c) and then comparing every O valency with the V_{Co} valencies, the local charge neutrality restricts possible candidates for the structural water site to only one O site, $W_O(6)$. Otherwise, the O6 atom becomes isolated OH^-.

(2-2) $V_{Co}(3/5/6)$-$W_O(7)$: Similar to the $V_{Co}(2/3/4)$ case, the $W_O(7)$ is the only possible O site for structural water, looking at the valencies of the Co3 and Co6 vacancies. (See Figure 2(d).)

Note that when optimizing these initial structural models by first-principles simulations (Subsection 2.5), the degree of spatial freedom is restricted such that H atoms in OH^-/H_2O are placed parallel/perpendicular to the *ab* plane, which avoids undesirable steric hindrance.

2.3. Hypothesis of the Deprotonation Reaction and EMF.
The electrochemical reaction of the CCH anode has been inferred from experiments based on cyclic voltammetry (CV) measurements.[3] The CV measurements have provided the reaction EMF by observing the CV peaks appearing in the potential window, $V < 0.6$ V versus the SCE potential reference. The result suggests the following deprotonation reaction:

$$Co(OH)_2 \rightleftharpoons CoOOH + H^+ + e^- \tag{1}$$
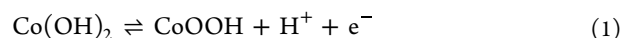
Equation 1 is an electrochemical (elementary) reaction of $Co(OH)_2$ rather than CCH itself, indicating that $Co(OH)_2$ forms in the CCH anode. The corresponding half-reaction in the CCH anode for *n* deprotons per unit cell ($1 \leq n \leq 6$) is given as

$$Co_6C_2O_{15}H_{10} + nOH^-$$
$$= Co_6C_2O_{15}H_{10-n} + nH_2O + ne^- + V_{CCH} \text{ (vs SHE)}$$
$$(2)$$
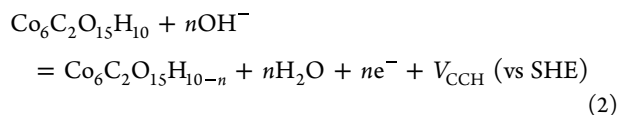
where V_{CCH} (vs SHE) is the CCH electrode potential versus the standard hydrogen electrode (SHE). Hereafter, all the electrochemical potentials are measured by referring to the SHE. For $n = 6$, all the Co^{2+} ions are oxidized to Co^{3+}, with the reaction rate being 1. The cathodic half-reaction is assumed to be the Pt electrode reaction in an alkaline solution (KOH):

$$nH_2O + ne^- = nOH^- + \frac{n}{2}H_2 + V_{Pt} \text{ (vs SHE)}$$
$$(3)$$
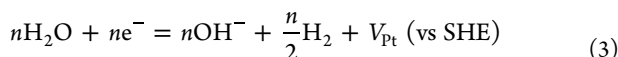
where V_{Pt} is the Pt electrode potential. Eventually, the overall reaction is obtained:

$$Co_6C_2O_{15}H_{10} = Co_6C_2O_{15}H_{10-n} + \frac{n}{2}H_2 + V_{dp} \text{ (vs SHE)}$$
$$(4)$$
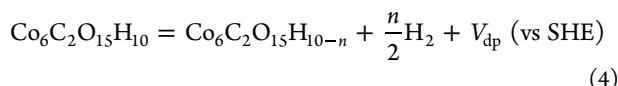
where V_{dp} is the deprotonation potential.

Herein, we establish relationships between the electrochemical potentials. The deprotonation potential in eq 4 is a sum of the anodic potential in eq 2 and the cathodic potential in eq 3:

$$V_{dp} = V_{CCH} + V_{Pt} \text{ (vs SHE)}$$
$$(5)$$

The V_{CCH} has been measured through the CV experiment as the peak of EMF, referring to the SCE potential.[20] We convert the experimentally set V_{CCH} (vs SCE) to a computationally tractable V_{CCH} (vs SHE) via

$$V_{CCH} \text{ (vs SHE)} = V_{CCH} \text{ (vs SCE)} + V_{SCE} \text{ (vs SHE)}$$
$$(6)$$

where V_{SCE} (vs SHE) is the SCE electrode potential measured via SHE. Substituting eq 5 with experimental values ($V_{SCE} = 0.2681$ V and $V_{Pt} = -0.8277$ V)[20] into eq 6, we obtain the EMF (vs SCE) for the CCH anode as

$$V_{CCH} \text{ (vs SCE)} = (V_{dp} - 1.0958) \text{ V (vs SHE)}$$
$$(7)$$

Thus, the V_{CCH} (vs SCE) value can be evaluated from the V_{dp} (vs SHE) value that can be computed via first-principles simulations, as shown in the next subsection.

2.4. First-Principles Evaluation of Deprotonation EMF and Oxidant Modeling. The V_{dp} value can be converted into the deprotonation energy, ΔE_{CCH}, for n deprotons, using

$$\Delta E_{dp} = nF \cdot V_{dp}$$
$$(8)$$

where F is the Faraday's constant. Referring to the overall reaction in eq 4, the ΔE_{CCH} is given as

$$\Delta E_{dp} = E_{CCH} - \left[E_{CCH-nH} + \frac{n}{2}E_{H_2} \right]$$
$$(9)$$

where E_{CCH} and E_{CCH-nH} are the total energies of the reductant (CCH) and the oxidant (CCH−nH) with n deprotons, respectively, and $\frac{n}{2}E_{H_2}$ is the chemical potential of the hydrogen atom.

Although the above three energies are computable, as shown in the next subsection, the evaluation of E_{CCH-nH} involves modeling the oxidant structure. In this study, we modeled the oxidant by removing one hydrogen atom ($n = 1$) from the most stable reductant, $V_{Co}(2/3/5)$. Ten possible deprotonation sites are shown in Figure 3. For our purpose, as shown later, the $n = 1$ case suffices to evaluate V_{dp}. Note that our concern is whether or
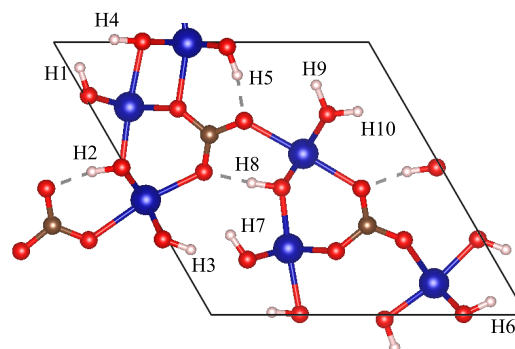
Figure 3. Deprotonation sites (H1∼H10) in the unit cell on the *ab* plane. Co, O, C, and H atoms are colored in blue, red, brown, and white, respectively.

not the deprotonation reaction occurs inside the CCH bulk. In other words, we are investigating whether or not V_{CCH} lies in the range of the experimental potential window, $V_{exp} < 0.6$ V (vs SCE).

2.5. First-Principles Geometry Optimization. Our first-principles simulations based on density functional theory (DFT) were performed using the Vienna ab initio simulation package (VASP).[21,22] The valence electron−core interactions were described by projector augmented wave (PAW),[23] where the valence electrons were treated as $Co(3s^74s^2)$, $O(2s^22p^4)$, $C(2s^22p^2)$, and $H(1s^1)$. We adopted the GGA-PBE exchange-correlation functional[24] and applied the GGA+U method to describe the localized Co-3d orbitals with the Hubbard correction value $U_{eff} = 6.1$ eV obtained from the value applied to cobalt oxide;[25] we also added the Grimme D3 correction[26] with the Beck−Johnson damping[27] to the GGA+U functional to reproduce the noncovalent interactions. The cutoff energy of the plane-wave basis expansion was set to 700 eV; a k-point mesh of $2 \times 2 \times 6$ was used for integration in the reciprocal lattice space using the Monkhorst−Pack scheme.[28] These values were found to converge within 1 meV/atom. The convergence criteria for the geometry optimization were set to 1×10^{-6} eV and 0.01 eV/Å for energy and force, respectively. All the lattice parameters were fixed to be the experimental values[13] during the geometry optimization; that is, only the atomic positions were optimized by our first-principles simulations. To accelerate the convergence in the geometry optimization, we first optimized the H positions, followed by all the atomic positions, which suppresses a high degree of spatial freedom in geometry optimization.

2.6. XRD Pattern Prediction. Previously, the XRD peaks of the CCH electrodes were incorrectly assigned to crystal plane indices because the CCH crystal structure was assumed to be an orthorhombic lattice.[14] To reassign the XRD peaks to plane indices of the hexagonal lattice, we performed XRD simulations for the computationally determined CCH hexagonal structure using the VESTA software.[19] As the strongest XRD peaks indicate the direction of the crystal growth, new XRD alignments can provide new insight into 1-D anisotropic CCH electrodes exhibiting high capacity.[3,12]

3. RESULTS
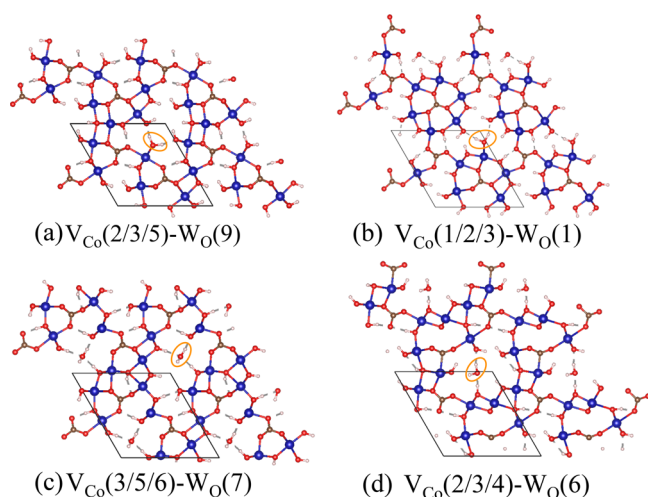
3.1. Identification of Reductant. To identify the reductant structure, we performed DFT simulations for all the possible arrangements of V_{Co} and H_2O, i.e., for the 14 patterns of $V_{Co}(i/j/k)$-$W_O(l)$ shown in Figure 2, followed by exploring the most stable one. Table 1 lists four pairs of the V_{Co} and W_O positions,

Table 1. Four V_{Co} Patterns in Figure 4 and the Corresponding Most Stable W_O Sites, Together with Their Relative Energies (ΔE)[a]

category	$V_{Co}(i/j/k)$	$W_O(l)$	ΔE/eV
1-1	2/3/5	9	+0.00
1-2	1/2/3	1	+0.47
2-1	3/5/6	7	+0.89
2-2	2/3/4	6	+5.42

[a]ΔE is set to be zero for $V_{Co}(2/3/5)$-$W_O(9)$.

and each of them provided the most stable structure among each category. The most stable structure among the four arrangements is set to be zero energy; the corresponding structures are shown in Figure 4. The most stable structure was (1-1) $V_{Co}(2/3/5)$-$W_O(9)$, where the V_{Co} positions are delocalized, as shown in Figure 4(a). This structure is stabilized by three hydrogen bonds: two are formed between two H atoms in OH and two O atoms in CO_3^{2-}, and one is formed around V_{Co} surrounded by two CO_3^{2-}. The second most stable structure is (1-2) $V_{Co}(1/2/3)$-$W_O(1)$, with only one hydrogen bond formed around one CO_3^{2-}. which is shown in Figure 4(b). Therefore, the energy of $V_{Co}(1/2/3)$-$W_O(1)$ is higher than that of $V_{Co}(2/3/5)$-$W_O(9)$ by 0.47 eV; as a result, it cannot be thermodynamically synthesized because of its synthesis temperature (368 K).[3] The other two localized structures, (2-1) $V_{Co}(3/5/6)$-$W_O(7)$ and (2-2) $V_{Co}(2/3/4)$-$W_O(6)$, have much higher energies than the most stable structure, (1-1) $V_{Co}(2/3/5)$-$W_O(9)$. This can be attributed to the fact that Coulomb repulsions between more localized V_{Co} pairs are greater than those between delocalized ones, irrespective of H-bonds.

Herein, we investigated the relative stability of $V_{Co}(2/3/5)$ with respect to different sites of H_2O, $W_O(l)$ ($l = 1-9$), listed in Table 2. The three structures, $V_{Co}(2/3/5)$-$W_O(6)/$-$W_O(1)/$-$W_O(5)$, are more stable than (1-2) $V_{Co}(1/2/3)$-$W_O(1)$, but less stable than (1-1) $V_{Co}(2/3/5)$-$W_O(9)$. $V_{Co}(2/3/5)$-$W_O(6)/$-$W_O(1)/$-$W_O(5)$ have higher energies than $V_{Co}(2/3/5)$-$W_O(9)$ by 0.15/0.32/0.42 eV, respectively. Similar to $V_{Co}(1/2/3)$-

Figure 4. Four reductant structures with delocalized (1-1/1-2) and localized (2-1/2-2) arrangements of Co vacancies, each of which is the most stable among their categories: (a) (1-1) $V_{Co}(2/3/5)$-$W_O(9)$, (b) (1-2) $V_{Co}(1/2/3)$-$W_O(1)$, (c) (2-1) $V_{Co}(3/5/6)$-$W_O(7)$, and (d) (2-2) $V_{Co}(2/3/4)$-$W_O(6)$. Positions of structural waters are encircled by orange-colored ellipses.

Table 2. Relative Stability of $V_{Co}(2/3/5)$ with Respect to Different Sites of H_2O, $W_O(l)$ ($l = 1-9$)[a]

$W_O(l)$	ΔE/eV
9	+0.00
6	+0.15
1	+0.32
5	+0.42
3	+0.51
7	+0.68
8	+0.96
2	+1.37
4	+5.47

[a]The relative energy ΔE is given in eV, setting the most stable $V_{Co}(2/3/5)$-$W_O(9)$ pattern to be zero.

$W_O(1)$, these metastable phases are not synthesized thermodynamically due to their synthesis temperatures. Three delocalized V_{Co} patterns, $V_{Co}(2/3/5)$-$W_O(2)/$-$W_O(4)/$-$W_O(8)$, are less stable than the localized $V_{Co}(3/5/6)$-$W_O(7)$ due to the presence of highly sterically hindered structural water sites. Thus, we conclude that the CCH reductant has the $V_{Co}(2/3/5)$-$W_O(9)$ structure, which is thermodynamically synthesizable. Its structural stability can be attributed to the above-mentioned H-bonds.

A validation of the V_{Co} and W_O arrangements in our predicted stable structure, $V_{Co}(2/3/5)$-$W_O(9)$, can be made by comparing with neutron diffraction (ND) experimental data. The W_O positions can be directly compared with the ND analysis,[29] whereas a reverse Monte Carlo analysis with the ND data is required to accurately determine the V_{Co} positions.[30] These ND-based analyses are required for validating our computational results, but ND experiments have yet to be reported, which we expect to appear in the near future.

3.2. Identification of Oxidant. To investigate the electrochemical reactivity of CCH, we obtained oxidant structures by removing H atoms from the reductant structure, $V_{Co}(2/3/5)$-$W_O(9)$, where the deprotonation sites (H_{dep}) are numbered as $H_1 \sim H_{10}$ in Figure 3. For computing the oxidant and reductant energies through DFT simulations, eq 8 is applied to evaluate the DFT-evaluated electromotive forces (EMFs) of the deprotonation reactions (V_{dep}^{DFT}) occurring inside CCH crystals, which are listed in Table 3. According to these computational results, all the deprotonation reactions require $V_{dep}^{DFT} \geq 3$ V. Compared with the computed EMFs, the experimental EMFs (V_{dep}^{exp}) are estimated to be less than +0.6 V because the CV measurements for the CCH capacitors report a potential

Table 3. DFT-Evaluated EMFs Required for the Deprotonation Reactions (V_{dep}^{DFT}) at Deprotonation Sites, H_{dep} (See Figure 3)

H_{dep}	V_{dep}^{DFT}/V (vs SCE)
7	3.05
10	3.08
3	3.08
2	3.26
1	3.27
8	3.30
6	3.34
9	3.52
4	4.06
5	4.89

window of $V_{dep}^{exp} < +0.6$ V when the deprotonation reaction occurs.

The difference between V_{dep}^{DFT} and V_{dep}^{exp} implies that the deprotonation reaction occurs not inside the CCH crystal, but on the surface. Note that V_{dep}^{DFT} approximates to a definite EMF (V_{dep}) because V_{dep} should be defined as the energy difference between the reductant and transition state in the electrochemical reaction (i.e., activation energy), whereas V_{dep}^{DFT} is just the energy difference between the reductant (before reaction) and oxidant (after reaction) energies, according to eq 8. However, because V_{dep}^{DFT} necessarily underestimates V_{dep}, the present V_{dep}^{DFT} values are sufficient to prove whether or not the deprotonation reaction occurs inside the CCH crystal. Actually, it is quite hard to perform exhaustive first-principles transition state calculations[17] for all the H_{dep} sites due to their computational costs.

Here we make a remark on our structural modeling for evaluating V_{dep}^{DFT}. The present study adopted only a unit cell of CCH to evaluate V_{dep}^{DFT}. This indicates that possible atomic configurations are quite limited. So one may wonder if other possible configurations could reduce the V_{dep}^{DFT} values. To verify this, we need to extend a simulation cell to supercell models involving many more possible atomic configurations, but such supercell simulations are impossible to run because of the computational cost. Such configurations are likely to reduce the V_{dep}^{DFT} values, but the reduction cannot reach $V_{dep}^{exp} \sim +0.6$ V (vs SCE) because the deprotonation inside the CCH bulk necessitates breaking both the H-bond and the O—H covalent bond, which involves high energy of an eV order. By inference, we may conclude that deprotonation rarely occurs inside the CCH bulk, compared to the surface.

Our computational results further suggest that a single phase of pristine CCH electrode has a low capacitance, which is consistent with experimental observations.[4] Although there is no direct experimental evidence that deprotonation rarely occurs inside the CCH bulk, our computational finding in the deprotonation is also likely in terms of the capacitance. To confirm if deprotonation occurs only on the surface from the computational viewpoint, deprotonation simulations on surfaces should be performed, which involves determining the stable surface of CCH and evaluating the EMFs based on the stable surface. As the CCH crystal structure including the Co vacancies and H atoms has a $P1$ symmetry, it is quite hard to cleave its typical surfaces. In addition, the resultant surfaces have too many atoms in their simulation cells to simulate because of computational costs. Thus, surface deprotonation simulations remain our future challenge. To summarize, the CCH bulk itself is stable against an electrochemical reaction; the electrochemical stability in the CCH bulk can be augmented by the H-bonds formed between all the H atoms and the neighboring O atoms, as shown in Figure 3.

In contrast to the pristine CCH electrode with low capacity, some CCH-based electrodes have been reported to exhibit high capacity.[3,12] The difference between high- and low-capacity CCH electrodes can be attributed to their different morphologies and constituent phases. According to experimental characterization,[3] high-capacity CCH electrodes consist of a pristine CCH phase and a hydroxide ($Co(OH)_2$) phase. Thus, we investigated the crystal growth mechanism of CCH based on XRD analysis, which is the key to understanding how actual CCH electrodes are synthesized.

3.3. Crystal Growth Designated by XRD Peaks. In terms of capacity, there are two types of CCH-based electrodes: CCH-

based electrodes with high capacity[3] and low capacity[4,11] are synthesized with NO_3^- and Cl^- counterions for cobalt ions (NA- and CA-CCH), respectively. They exhibit different morphologies that arise from different crystal growth directions and degrees of crystallinity. Differences in the crystal growth directions and degrees of crystallinity for CCH can be explained using the observed XRD patterns.

In fact, previous studies characterized XRD patterns of the CCH-based electrodes, but their XRD analyses were based on an incorrect lattice ansatz, an orthorhombic lattice.[14] The correct lattice of CCH was recently found to be a hexagonal lattice.[13] Note that the crystal growth direction of a pristine CCH crystal was found to be the c-axis. Thus, the XRD patterns of the actual CCH electrodes should be reassigned into Miller indices.

In order to correctly assign XRD peaks to Miller indices, we performed an XRD simulation based on the correct CCH crystal structure obtained computationally, where its unit cell came from NA-CCH,[13] and the occupancy of the structural water site was set to be 1.0. Note that our assignment of lattice planes differed from the previous study,[18] because the correct CCH structure is different than that previously characterized. Then, we examined which plane contributes to the morphology difference of NA- and CA-CCH electrodes from the XRD simulation results. It is well-known that an XRD peak position (2θ) identifies certain lattice planes, whereas the relative peak intensity shows the amount of said planes formed in a sample material. Figure 5 shows the XRD peaks in terms of relative intensity, where the strongest value is set to 100.
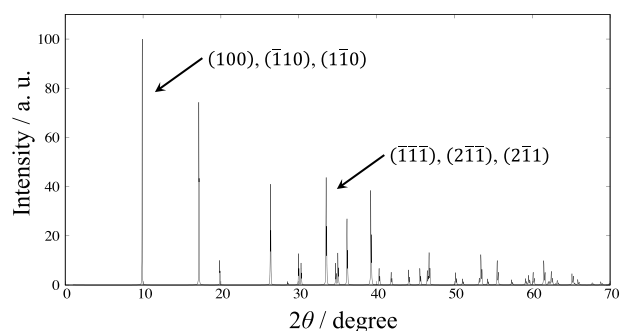
Figure 5. XRD peak pattern obtained from the XRD simulation for the computed hexagonal CCH crystal structure (3-D NA-CCH). The peaks at $2\theta = 9.885$ and 33.515 include plane sets $\{(100), (\bar{1}10), (1\bar{1}0)\}$ and $\{(\bar{1}\bar{1}\bar{1}), (2\bar{1}\bar{1}), (2\bar{1}1)\}$, respectively. They were incorrectly assigned in previous studies, because the crystal structure was assumed to be orthorhombic and not hexagonal.

Here we focus on the two peaks at $2\theta = 9.885$ and 33.515; the former is related to the crystal growth direction almost parallel to the c-axis, whereas the latter was toward the ab-plane, as shown below. Note that each of the peaks consists of several lattice planes with different intensities, but our concern is only the main peaks with intensities higher than 20% of the strongest intensity. Eventually, the peaks at $2\theta = 9.885$ and 33.515 correspond to sets of lattice planes (1) $\{(100), (\bar{1}10), (1\bar{1}0)\}$ and (2) $\{(\bar{1}\bar{1}\bar{1}), (2\bar{1}\bar{1}), (2\bar{1}1)\}$, respectively; their structures are given in the Supporting Information (SI). Note that only representative lattice planes appear in Figure 5, whereas their equivalent planes are omitted. (1) Looking at the former planes, we can see that H-bonds (encompassed with green rectangles)

formed on the *ab*-planes connecting the (100) planes (Figure S1). These H-bonds can promote 2-D crystal growth (*a*- and *b*-axis directions). The above finding is similar to the $(1\overline{1}0)$ and $(\overline{1}10)$ planes. (2) For the latter, H-bonds are formed so as to connect the $(\overline{1}\,\overline{1}\,\overline{1})$ planes, whose direction is almost parallel to the *c*-axis (Figure S2). These H-bonds can work for 1-D crystal growth (*c*-axis direction), which can be called "H-bond-driven 1-D crystal growth". This holds for the $(2\overline{1}\,\overline{1})$ and $(2\overline{1}1)$ planes as well. Thus, a comparison between $I(9.885)$ and $I(33.515)$ can provide insights into the crystal growth direction.

The NA- and CA-CCH electrodes have different surfaces with specific lattice planes, which is caused by the difference in their different crystal growth directions. To investigate this difference, we make a comparison of their intensities. For that purpose, we adopt a ratio of the peak intensity at $2\theta = 33.515$ to that at $2\theta = 9.885$:

$$R = \frac{I(33.515)}{I(9.885)} \tag{10}$$

Recall that the simulated XRD peaks are computed for an isotropic CCH bulk. By contrast, anisotropic CCH electrodes have differing $I(2\theta)$ values from the bulk, though they have the same 2θ as the bulk. Thus, the NA-CCH and CA-CCH electrodes have different R values from the bulk. Table 4 lists

Table 4. Peak Intensities $I(2\theta)$ at $2\theta = 9.885$ and 33.515, and the Corresponding Intensity Ratio R for the NA- and CA-CCH Electrode Materials and the Bulk[a]

	$I(9.885)$	$I(33.515)$	R
NA-CCH[18]	≃60	≃100	≃1.7
CA-CCH[18]	≃80	≃35	≃0.44
bulk NA-CCH (present study)	100	44	0.44

[a]The $I(2\theta)$ values for the NA- and CA-CCH materials were obtained from ref 18, whereas the corresponding bulk NA-CCH values are from the present XRD simulations.

$I(2\theta)$ at $2\theta = 9.885$ and 33.515 and R for the bulk and the NA- and CA-CCH electrodes (obtained from Figure 1(b) in ref 18). It was found that the NA- and CA-CCH electrodes have $R \simeq 1.7$ and ≃0.44, respectively. As we mentioned previously, relatively stronger peaks correspond to a higher amount of the corresponding planes compared to the others formed in a material. Thus, the plane set $\{(\overline{1}\,\overline{1}\,\overline{1}), (2\overline{1}\,\overline{1}), (2\overline{1}1)\}$ formed more than the set $\{(100), (\overline{1}10), (1\overline{1}0)\}$ in NA-CCH. This means that NA-CCH exhibits 1-D crystal growth toward the *c*-axis. By contrast, $\{(100), (\overline{1}10), (1\overline{1}0)\}$ formed more than $\{(\overline{1}\,\overline{1}\,\overline{1}), (2\overline{1}\,\overline{1}), (2\overline{1}1)\}$ in CA-CCH, indicating that the crystal growth direction of CA-CCH is more 2-D than that of NA-CCH. Here, we also see that the R value of CA-CCH is almost the same as that of the bulk NA-CCH. This indicates that in CA-CCH, the 1-D crystal growth toward the *c*-axis is balanced with the 2-D growth inside *ab*-planes. In other words, the CA-CCH structure is 3-D, similar to the bulk NA-CCH structure. To sum up, the NA-CCH electrode is 1-D, whereas the CA-CCH electrode is 3-D, which can be attributed to the H-bonds formed therein.

We have investigated why the directions of H-bonds in NA-CCH are different from those in CA-CCH. NO_3^- and Cl^- are used as cobalt counteranions to synthesize NA- and CA-CCH, respectively. Their difference in reactants gives rise to that in the occupancy of structural water groups[18] It has been observed

experimentally that NA-/CA-CCH with a higher/lower H_2O occupancy grows one-/two-dimensionally, implying that the structural water groups inhibit 2-D crystal growth.[18] As shown in Figure S2, a structural water group (encompassed with an orange ellipse) forms two H-bonds between the $(\overline{1}\,\overline{1}\,\overline{1})$ planes. The *c*-axis H-bond involving the structural water group is considered to promote one-dimensional crystal growth of NA-CCH. By contrast, the structural water group in CCH can be regarded as a growth inhibitor in the 2-D direction.

In addition to the peak intensities, peak broadening provides an insight into the capacitance difference between the NA- and CA-CCH electrodes. NA-CCH was found to have broad peaks in the overall angle range.[18] The presence of these broad peaks can be attributed to the size of the crystals and defects in the NA-CCH electrodes. The $Co(OH)_2$ phase is present in the NA-CCH electrode.[3] As the NA-CCH crystal growth direction is toward the *c*-axis,[13] $Co(OH)_2$ layers are anisotropically stacked along the *c*-axis direction when synthesizing the NA-CCH electrode with CCH precursors. The $Co(OH)_2$ is considered to be the β phase: it has two polymorphs, α/β-$Co(OH)_2$, where the α phase is metastable and transformed easily into the β phase.[31] This indicates that β-$Co(OH)_2$ rather than α-$Co(OH)_2$ is synthesized using the CCH precursor. Thus, we focused on the crystal growth and electrochemical reaction of the pristine β-$Co(OH)_2$ phase as well. The pristine β-$Co(OH)_2$ crystal has pore layers, and hence, OH^- ions enter through these pore layers, thereby leading to the deprotonation reaction in the crystal. By contrast, it has been observed from TEM images that plate surfaces come in contact with interlayers during crystal growth to form the aggregated bulk electrode; that is, thick plate structures of β-$Co(OH)_2$ aggregate into the β-$Co(OH)_2$ bulk electrode.[8] The contact site of the interlayer and plate surface can prevent OH^- ions from entering into the interlayer where the deprotonation reaction occurs. The $Co(OH)_2$ phase is formed from the crystal surface via a decarboxylation reaction between CCH and OH^-. The pore layers of the deprotonation sites in the β-$Co(OH)_2$ are oriented toward the electrolyte. Eventually, more anisotropic β-$Co(OH)_2$ is synthesized than pristine β-$Co(OH)_2$.

4. DISCUSSION

4.1. Morphology-Driven Storage Properties. Table 5 lists storage properties (capacity and cycle life) of high- and low-capacity CCH electrodes, NA-CCH[3] and CA-CCH,[4,11] as well as pristine α/β-$Co(OH)_2$ electrodes for comparison, which have been reported in previous studies. Their differences can be interpreted in terms of their morphologies, as shown below.

First, we investigated the CA-CCH electrodes. As mentioned previously, the CA-CCH electrodes are composed of single crystals, where the $Co(OH)_2$ phases hardly exist inside the crystal. In addition, the CA-CCH electrodes have fewer defects and smaller surface areas (relative to the bulk region) than NA-CCH. This implies that OH^- ions in the electrolytic solution are hindered from diffusing into the inside region in the CCH crystal. In other words, the OH^- ion diffusions only occur in restricted surface areas. These conjectures would give rise to the low capacitance of 165 F/g in the CCH electrode aggregated on a stainless-steel substrate, forming nanorod-assembled hierarchical structures,[4] as shown in Table 5. This assembled structure consists of a 1-D aggregated rod, whereas each rod unit is two-dimensionally grown. The 2-D morphology causes the deprotonation reaction to occur only on the surface regions;

Table 5. Capacitance and Cycle Characteristics of Co-Based Electrode Materials, Associated with Morphologies[a]

electrode	morphology	capacity@[electron density]/ $Fg^{-1}@Ag^{-1}$	cycle life@ [charge density]/ (cycles)/%@Ag^{-1}
NA-CCH@ NF[b]	umbrella-like NWA	1227[@2.25]	93.7[@4.0](10000)
NA-CCH@ NF[c]	umbrella-like NWA	1381[@2.0]	93.5[@40.0](5000)
CA-CCH@ SS[d]	nanorod-assembled	165.6[@0.1]	~100.0[@0.5](1000)
α-Co(OH)$_2$@ NF[e]	porous film	1473[@2.0]	88.0[@6](1000)
β-Co(OH)$_2$@ CFP[f]	nano plate	800[@2.0]	95.7[@2](8000)

[a]CFP, NF, SS, and PN indicate substrates of carbon fiber paper, nickel foam, stainless steel, and porous Ni, respectively. [b]Cathode: Pt foil, Anode: CCH, Reference electrode: Hg/HgO.[12] [c]Cathode: Pt, Anode: CCH, Reference electrode: SCE.[3] [d]Cathode: Pt foil, Anode: CCH, Reference electrode: Hg/HgO.[4] [e]Cathode: Pt plate, Anode: α-Co(OH)$_2$, Reference electrode: SCE.[7] [f]Cathode: Pt plate, Anode: β-Co(OH)$_2$, Reference electrode: SCE.[8]

therefore, the reaction becomes reversible, leading to the "perfect" cycle life, as shown in Table 5.

By contrast, the NA-CCH electrodes have significantly different morphologies compared to the CA-CCH ones: NA-CCH is composed of not only CCH but also Co(OH)$_2$ phases, that is, it is multiphase, with small crystal sizes and defects, compared to NA-CCH.[3,12,18] The smaller crystal sizes lead to wider surface areas compared to the bulk region, increasing the diffusion sites of OH$^-$ ions on the surface and hence forming the Co(OH)$_2$ phase. The surface defects and grain boundaries also enhance the diffusion of OH$^-$ inside the single crystals and on the single-crystal surfaces located in the polycrystals. Specifically, grain boundaries may promote the formation of the Co(OH)$_2$ phase. Eventually, the high capacity of NA-CCH can be attributed to the above-mentioned characteristic morphologies. The 1-D morphology enhances the deprotonation reaction occurring at the Co(OH)$_2$ phases. Therefore, the NA-CCH morphology leads to higher capacity, but a lower life cycle, compared to those of CA-CCH. However, NA-CCH partially contains the CCH phase, which makes the electrode more stable than the pristine Co(OH)$_2$ phase. This is the reason why NA-CCH has longer life cycles (~93%) than the pristine α-Co(OH)$_2$ electrode. By contrast, the pristine β-Co(OH)$_2$ electrode has longer life cycles (~96%) than the NA-CCH electrodes (~94%), but in turn, it has a significantly lower capacity (800 F/g). In general, there exists a counterbalance between capacity and life cycle.

Herein, we remark on how electrolytes affect the growth mechanism of CCH-based electrode materials, which significantly governs the balance between CCH and Co(OH)$_2$ phases. First, we focus on concentrations of OH$^-$ and CO_3^{2-} that commonly exist in reaction systems during the synthesis of NA-/CA-CCH electrode materials. OH$^-$ ions are common to the syntheses of Co(OH)$_2$ and CCH, whereas CO_3^{2-} ions exist only in the synthesis of CCH. Thus, denser OH$^-$ ions seem to contribute to a larger ratio of the Co(OH)$_2$ phase to the CCH phase, thereby leading to more deprotonation. pH-controlled experiments on crystal growth would easily confirm this, though such experiments have yet to be conducted.

Next, we consider the NO$_3^-$ and Cl$^-$ electrolytes. Compared with OH$^-$ and CO_3^{2-}, they play a more important role in synthesizing the CCH-based electrode materials, NA-/CA-CCH. It has been experimentally shown that the NA-CCH electrode consists of a mixture of CCH and Co(OH)$_2$ compounds, whereas the CA-CCH electrode consists of not only CCH and Co(OH)$_2$, but also Co(OH)$_x$Cl$_{2-x}$·nH$_2$O and Co(OH)$_x$Cl$_y$(CO$_3$)$_{0.5}$(2 − x − y)·nH$_2$O compounds.[18] These chloride-containing compounds fail to work for the electrochemical reaction. Elemental analysis has confirmed that the CA-CCH electrode contains more OH ions than the NA-CCH electrode, and the case of CO$_3$ ions is the opposite.[18] Despite the increased amount of OH ions in the CA-CCH electrode, the CA-CCH electrode has a low capacitance, compared to that of the NA-CCH electrode. This implies that the OH ions are assigned into the chloride-containing compounds more than the Co(OH)$_2$ and the CCH. Furthermore, the lower CO$_3$ concentration in the CA-CCH indicates that fewer decarboxylation reactions occur during the charge−discharge cycle,[4] which hinders capacitance increases that have been observed in the NA-CCH electrodes.[3,12] Thus, the lower capacity in the CA-CCH can be attributed to the presence of chloride-containing compounds.

To understand the above-mentioned difference between NO$_3^-$ and Cl$^-$ electrolytes, a key quantity is electron affinity (EA). The experimental EA values of NO$_3^-$ and Cl$^-$ have been reported to be −76.5 and −59.2 kcal/mol, respectively.[32] This means that NO$_3^-$ ions exist in solution, whereas Cl$^-$ ions tend to bind with the cations, thereby getting involved in the crystal growth mechanism. Therefore, chloride-containing compounds can be formed in CA-CCH electrode materials. In other words, the NO$_3^-$ electrolyte forms only CCH and Co(OH)$_2$. By considering the EA of electrolytes, we can control the balance between the CCH and Co(OH)$_2$.

4.2. Further Details for NA-CCH. Within the framework of the NA-CCH electrodes, their morphologies significantly vary depending on their growth times, which affects their storage performance. For instance, as per Lin et al.,[3] the CCH precursors were grown on NF substrates and the morphologies of the NA-CCH electrodes controlled the growth times of 6 and 10 h (designated as NA-CCH@NF-6h and NA-CCH@NF-10h, respectively). Both electrodes have wire structures having larger surface areas perpendicular to their substrates, compared to the CA-CCH electrodes. However, upon comparing them, a remarkable difference in the wire orientations was found relative to the substrate.

NA-CCH@NF-10h has an umbrella-like nanowire structure, which corresponds to that listed in Table 5. By contrast, NA-CCH@NF-6h has a nanoneedle structure oriented perpendicular to the substrate. According to experimental observations based on XRD and TEM, the NA-CCH@NF-6h structure is more uniaxially anisotropic than the NA-CCH@NF-10h one, and hence, the former has wider surface areas on the sides perpendicular to the substrate than the latter.

Their structural/morphological difference results in a difference in storage performance. NA-CCH@NF-6h has a higher capacity (1548 F/g(@2 A/g)) Than that of NA-CCH@NF-10h (1381 F/g(@2 A/g)) at the initial stage of the charge−discharge cycle. This can be explained as follows: NA-CCH@NF-6h and NA-CCH@NF-10h are almost identical to each other in terms of the broadness of the XRD peak patterns. This implies that they have almost identical defect structures. Therefore, the capacity difference between NA-CCH@NF-6h and NA-CCH@

NF-10h can be attributed to the difference in their surface areas; during the initial cycles, the OH^- ions react with the CCH surface and further diffuse into the inside crystal. This reaction in NA-CCH@NF-6h enhances the capacity, but rapidly degrades the cycle stability, giving rise to the deformation of the structure. Because of its 1-D morphology, the unstable structure in NA-CCH@NF-6h can be attributed to fewer hydrogen bonds and chemical bonds with CO_3^{2-} than in the pristine CCH crystal (Figure 2(a)). In the middle stage of the charge−discharge cycle, the structural change inhibits the OH^- ions from diffusing into the interlayers inside the crystal. Finally, the NA-CCH@NF-6h electrode melts down, losing storage performance.

Recently, the storage performance has been reported for a CCH electrode similar to NA-CCH@NF-10h, exhibiting a high capacity of 1227 F/g(@2.25 A/g) and high cycle stability of 93.7% (@4 A/g) after 10,000 cycles.[12] The CCH phase contributes to the cycle stability due to its hydrogen and chemical bonding, whereas the $Co(OH)_2$ phase enhances the capacity albeit with less stability. The above-mentioned high performance was achieved by counterbalancing the two phases. This study has highlighted the possibility of regulating the ratio of the CCH phase to the $Co(OH)_2$ phase by controlling the reaction surface area.

5. CONCLUSION

We performed exhaustive first-principles simulations to identify a hexagonal CCH structure, particularly for the atomic positions of cobalt vacancies and hydrogen atoms. The resultant structure is a model of the reductant in the electrochemical reaction of CCH-based electrodes. This was used to explore the oxidant structure. The reductant and oxidant structures helped us to evaluate the EMF of the deprotonation reaction. The computed EMF value of ~3 V (vs SCE) was much larger than that expected from the experimental potential window of <0.6 V (vs SCE). This indicates that the deprotonation reaction never occurs inside the CCH bulk, and therefore, the reaction sites are restricted to the surface regions in the pristine CCH electrode. The detailed information about the atomic positions revealed that the chemical and hydrogen bonds that formed between the $\{(\overline{1}\,\overline{1}\,\overline{1}), (2\,\overline{1}\,\overline{1}), (2\,\overline{1}\,1)\}$ planes prevent the hydroxide (OH^-) ions from diffusing into the inside of the crystal. We also performed an XRD simulation to assign XRD peaks to the Miller indices based on the computed structure with the correct hexagonal lattice. The reassigned Miller indices revised the crystal growth direction to be specified by the $\{(\overline{1}\,\overline{1}\,\overline{1}), (2\,\overline{1}\,\overline{1}), (2\,\overline{1}\,1)\}$ planes.

According to the above-mentioned computational findings, we investigated how certain CCH electrodes achieve a better storage performance than pristine $Co(OH)_2$ electrodes. The revised crystal growth direction clarified the morphologies formed in the high-capacity CCH electrode synthesized with the NO_3^- counterion. These results help us understand the importance of both counterbalancing the coexisting CCH and $Co(OH)_2$ phases and controlling their morphologies (e.g., forming an umbrella-like morphology) for achieving the best storage performance.

ASSOCIATED CONTENT

Ⓢⓘ Supporting Information

The Supporting Information is available free of charge at https://pubs.acs.org/doi/10.1021/acsomega.2c07362.

Supporting figures: Hydrogen-bond sites between each lattice plane, which promote 1-dimensional crystal growth (PDF)

■ AUTHOR INFORMATION

Corresponding Authors

Kenji Oqmhula − *School of Information Science, Japan Advanced Institute of Science and Technology, Nomi, Ishikawa 923-1292, Japan;* ⓞ orcid.org/0000-0003-0271-3525; Email: mwkokk1907@icloud.com

Kenta Hongo − *Research Center for Advanced Computing Infrastructure, JAIST, Nomi, Ishikawa 923-1292, Japan;* ⓞ orcid.org/0000-0002-2580-0907; Email: kenta_hongo@mac.com

Authors

Takahiro Toma − *School of Information Science, Japan Advanced Institute of Science and Technology, Nomi, Ishikawa 923-1292, Japan*

Ryo Maezono − *School of Information Science, Japan Advanced Institute of Science and Technology, Nomi, Ishikawa 923-1292, Japan;* ⓞ orcid.org/0000-0002-5875-971X

Complete contact information is available at: https://pubs.acs.org/10.1021/acsomega.2c07362

Notes

■ ACKNOWLEDGMENTS

■ REFERENCES

(1) Fleischmann, S.; Mitchell, J. B.; Wang, R.; Zhan, C.; Jiang, D.; Presser, V.; Augustyn, V. Pseudocapacitance: From Fundamental Understanding to High Power Energy Storage Materials. *Chem. Rev.* **2020**, *120*, 6738−6782.

(2) Liang, R.; Du, Y.; Xiao, P.; Cheng, J.; Yuan, S.; Chen, Y.; Yuan, J.; Chen, J. Transition Metal Oxide Electrode Materials for Supercapacitors. *A Review of Recent Developments* **2021**, *11*, 1248.

(3) Lin, X.; Li, H.; Musharavati, F.; Zalnezhad, E.; Bae, S.; Cho, B.-Y.; Hui, O. K. S. Synthesis and characterization of cobalt hydroxide carbonate nanostructures. *RSC Adv.* **2017**, *7*, 46925−46931.

(4) Shu, C.; Liang, Y.; Zhang, Z.; Fang, B. Synthesis and Electrochemical Properties of Hierarchical Porous (Nickel/Cobalt)-Carbonate-Hydroxide Structures. *Eur. J. Inorg. Chem.* **2021**, *2021*, 1659−1669.

(5) Deng, M.-J.; Huang, F.-L.; Sun, I.-W.; Tsai, W.-T.; Chang, J.-K. An entirely electrochemical preparation of a nano-structured cobalt oxide electrode with superior redox activity. *Nanotechnology* **2009**, *20*, 175602.

(6) Mirzaeian, M.; Akhanova, N.; Gabdullin, M.; Kalkozova, Z.; Tulegenova, A.; Nurbolat, S.; Abdullin, K. Improvement of the

Pseudocapacitive Performance of Cobalt Oxide-Based Electrodes for Electrochemical Capacitors. *Energies* **2020**, *13*, 5228.

(7) Kong, L.-B.; Liu, M.-C.; Lang, J.-W.; Liu, M.; Luo, Y.-C.; Kang, L. Porous cobalt hydroxide film electrodeposited on nickel foam with excellent electrochemical capacitive behavior. *Journal of Solid State Electrochemistry* **2011**, *15*, 571−577.

(8) Deng, T.; Zhang, W.; Arcelus, O.; Kim, J.-G.; Carrasco, J.; Yoo, S. J.; Zheng, W.; Wang, J.; Tian, H.; Zhang, H.; Cui, X.; Rojo, T. Atomic-level energy storage mechanism of cobalt hydroxide electrode for pseudocapacitors. *Nat. Commun.* **2017**, *8*, DOI: 10.1038/ncomms15194

(9) Ji, X.; Cheng, S.; Yang, L.; Jiang, Y.; Jiang, Z.; Yang, C.; Zhang, H.; Liu, M. Phase transition−induced electrochemical performance enhancement of hierarchical CoCO3/CoO nanostructure for pseudo-capacitor electrode. *Nano Energy* **2015**, *11*, 736−745.

(10) Choi, B. G.; Yang, M.; Jung, S. C.; Lee, K. G.; Kim, J.-G.; Park, H.; Park, T. J.; Lee, S. B.; Han, Y.-K.; Huh, Y. S. Enhanced Pseudocapacitance of Ionic Liquid/Cobalt Hydroxide Nanohybrids. *ACS Nano* **2013**, *7*, 2453−2460.

(11) Ghosh, D.; Mandal, M.; Das, C. K. Solid State Flexible Asymmetric Supercapacitor Based on Carbon Fiber Supported Hierarchical Co(OH)xCO3 and Ni(OH)2. *Langmuir* **2015**, *31*, 7835−7843.

(12) Liu, Q.; Chen, Y.; Ma, J.; Xiong, X.; Zeng, X.; Qian, H. Novel electrochemical deposition of Co(CO3)0.5(OH)·0.11H2O nano-needles with folded umbrella-like architecture onto nickel foam for supercapacitors. *Surface and Coatings Technology* **2021**, *421*, 127452.

(13) Bhojane, P.; Le Bail, A.; Shirage, P. M. A quarter of a century after its synthesis and with > 200 papers based on its use, 'Co(CO3)0.5(OH) · 0.11H2O' proves to be Co6(CO3)2(OH)8 · H2O from synchrotron powder diffraction data. *Acta Crystallographica Section C Structural Chemistry* **2019**, *75*, 61−64.

(14) Porta, P.; Dragone, R.; Fierro, G.; Inversi, M.; Jacono, M. L.; Moretti, G. Preparation and characterisation of cobalt−copper hydroxysalts and their oxide products of decomposition. *J. Chem. Soc., Faraday Trans.* **1992**, *88*, 311−319.

(15) Simon, P.; Gogotsi, Y. *Materials for electrochemical capacitors* **2008**, *7*, 845−854.

(16) Kim, C.; Kim, I.; Kim, H.; Sadan, M. K.; Yeo, H.; Cho, G.; Ahn, J.; Ahn, J.; Ahn, H. A self-healing Sn anode with an ultra-long cycle life for sodium-ion batteries. *J. Mater. Chem. A* **2018**, *6*, 22809−22818.

(17) Toma, T.; Maezono, R.; Hongo, K. Electrochemical Properties and Crystal Structure of Li⁺/H⁺ Cation-Exchanged LiNiO₂. *ACS Appl. Energy Mater.* **2020**, *3*, 4078−4087.

(18) Xu, R.; Zeng, H. C. Dimensional Control of Cobalt-hydroxide-carbonate Nanorods and Their Thermal Conversion to One-Dimensional Arrays of Co3O4 Nanoparticles. *J. Phys. Chem. B* **2003**, *107*, 12643−12649.

(19) Momma, K.; Izumi, F. *VESTA 3* for three-dimensional visualization of crystal, volumetric and morphology data. *J. Appl. Crystallogr.* **2011**, *44*, 1272−1276.

(20) *CRC Handbook, CRC Handbook of Chemistry and Physics*, 88th ed.; CRC Press, 2007.

(21) Kresse, G.; Furthmüller, J. Efficient iterative schemes for ab initio total-energy calculations using a plane-wave basis set. *Phys. Rev. B* **1996**, *54*, 11169−11186.

(22) Kresse, G.; Joubert, D. From ultrasoft pseudopotentials to the projector augmented-wave method. *Phys. Rev. B* **1999**, *59*, 1758−1775.

(23) Blöchl, P. E. Projector augmented-wave method. *Phys. Rev. B* **1994**, *50*, 17953−17979.

(24) Perdew, J. P.; Burke, K.; Ernzerhof, M. Generalized Gradient Approximation Made Simple. *Phys. Rev. Lett.* **1996**, *77*, 3865−3868.

(25) Wdowik, U. D.; Parlinski, K. Lattice dynamics of CoO from first principles. *Phys. Rev. B* **2007**, *75*, 104306.

(26) Grimme, S.; Antony, J.; Ehrlich, S.; Krieg, H. A consistent and accurate ab initio parametrization of density functional dispersion correction (DFT-D) for the 94 elements H-Pu. *J. Chem. Phys.* **2010**, *132*, 154104.

(27) Johnson, E. R.; Becke, A. D. A post-Hartree-Fock model of intermolecular interactions: Inclusion of higher-order corrections. *J. Chem. Phys.* **2006**, *124*, 174104.

(28) Monkhorst, H. J.; Pack, J. D. Special points for Brillouin-zone integrations. *Phys. Rev. B* **1976**, *13*, 5188−5192.

(29) Purevjav, N.; Okuchi, T.; Tomioka, N.; Wang, X.; Hoffmann, C. Quantitative analysis of hydrogen sites and occupancy in deep mantle hydrous wadsleyite using single crystal neutron diffraction. *Sci. Rep* **2016**, *6*, DOI: 10.1038/srep34988

(30) KITAMURA, N.; ISHIDA, N.; IDEMOTO, Y. Atomic-Configuration Analysis on LiNi₀.₅Mn₀.₅O₂ by Reverse Monte Carlo Simulation. *Electrochemistry* **2016**, *84*, 789−792.

(31) Gaunand, A.; Lim, W. From amorphous precipitates to sub-micronic crystalline platelets of Co(OH)2: a kinetic study of the transformation process. *Powder Technol.* **2002**, *128*, 332−337.

(32) Pritchard, H. O. The Determination of Electron Affinities. *Chem. Rev.* **1953**, *52*, 529−563.